Chinese Journal of Catalysis 34 (2013) 876–888
催化学报 2013年 第34卷 第5期 | www.chxb.cn

available at www.sciencedirect.com

ScienceDirect

journal homepage: www.elsevier.com/locate/chnjc

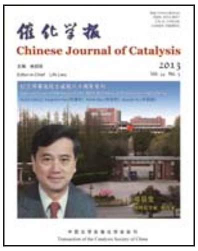

Article (Special Issue in Memory of the 80th Birthday of Professor Jingfa Deng)

Catalytic performance of different types of iron zeolites in N_2O decomposition

WANG Junying [a,b], XIA Haian [a], JU Xiaohua [a], FAN Fengtao [a], FENG Zhaochi [a], LI Can [a,*]

[a] *State Key Laboratory of Catalysis, Dalian Institute of Chemical Physics, Chinese Academy of Sciences, Dalian 116023, Liaoning, China*
[b] *Graduate University of Chinese Academy of Sciences, Beijing 100049, China*

ARTICLE INFO

Article history:
Received 26 December 2012
Accepted 24 February 2013
Published 20 May 2013

Keywords:
Iron
Zeolite
Nitrous oxide decomposition
Raman spectroscopy

ABSTRACT

A series of Fe/zeolites (ZSM-35, ZSM-5, beta, and mordenite) samples with Fe/Al molar ratios of 0.33 were prepared using a solid-state ion-exchange method. A combination of ultraviolet-visible diffuse reflectance, in-situ Fourier-transform infrared, and in-situ visible Raman spectroscopic techniques, with a transient response method, was used to investigate the influence of the zeolite framework on the catalytic properties of the Fe/zeolites in N_2O decomposition. The results show that the catalytic activity of the Fe/zeolites-HT (HT denotes high-temperature treatment) samples is in the order Fe/ZSM-35-HT > Fe/beta-HT > Fe/ZSM-5-HT > Fe/mordenite-HT. There is a linear relationship between the rate of N_2O decomposition and the concentration of binuclear iron sites. This indicates that binuclear iron sites are the active sites for N_2O decomposition. A correlation between the formation of binuclear iron sites and Fe ion distribution among the cationic sites is proposed. Two Fe(II) cations located in two adjacent six-membered rings in a 10-membered ring channel (α sites) or in two neighboring six-membered rings in an eight-membered ring channel (β sites) of Fe/ZSM-35 are favorable for the formation of active binuclear iron sites. Similar structure can also be formed in two adjacent six-membered rings in polymorphs A and B of beta zeolite or in the six-membered rings at the intersection of the straight and sinusoidal channels of the ZSM-5 framework. For the Fe/mordenite-HT sample, most of the iron species are present as isolated iron cations, so it has the lowest activity in N_2O decomposition.

1. Introduction

Iron-containing zeolites are known to be excellent catalysts for the decomposition of harmful N_2O to nitrogen and oxygen [1,2]. Since the early work performed in Panov's laboratory, Fe/ZSM-5 has been extensively studied experimentally and theoretically [3–6]. The experimental and theoretical studies have concentrated on the influence of the preparation method and the mode of pretreatment on the structure and properties of the active sites in Fe/ZSM-5 catalysts [3–6]. Far fewer studies have investigated the decomposition of N_2O over other Fe/zeolite samples [7–13].

Øygarden et al. [7] found that the activity of commercial BEA zeolite in direct N_2O decomposition was higher than those of FER and MFI; all have iron impurities. This is probably a result of the displacement of Fe and Al from the lattice, resulting in the formation of active bi- and oligo-nuclear iron sites. Kaucký et al. [8] reported that the shorter Fe–Fe distances in

---

* Corresponding author. Tel: +86-411-84379070; Fax: +86-411-84694447; E-mail: canli@dicp.ac.cn

This work was supported by the National Natural Science Foundation of China (21173213) and the National Basic Research Program of China (973 Program, 2009CB623507).

DOI: 10.1016/S1872-2067(12)60555-5 | http://www.sciencedirect.com/science/journal/18722067 | Chin. J. Catal., Vol. 34, No. 5, May 2013

Fe/FER cause higher activity in N_2O decomposition compared with that of Fe/beta. On the basis of spectroscopic techniques and density functional theory calculations, Jíša et al. [9,10] provided evidence that two Fe(II) cations accommodated in two adjacent six-membered rings in the eight-membered ring channel of Fe/ferrierite were probably responsible for its superior activity compared with Fe/beta and Fe/MFI in N_2O decomposition. An advantage of Fe/FER over Fe/BEA, Fe/ZSM-5, and Fe/FAU was found by Pantu et al. [11] and was ascribed to the smaller pores and slightly stronger adsorption properties of N_2O on FER zeolite. In a comparison of Fe/MFI and Fe/BEA with similar iron species, Pérez-Ramírez et al. [12] claimed that the microporous matrix does not play a decisive role in direct N_2O decomposition. Melián Cabrera et al. [13] reported that the activity of Fe/FER was better than those of Fe/MFI and Fe/BEA in the simulated tail gas of nitric acid plants; this probably originated from the generation and stabilization of active iron sites in Fe/FER. However, little information is available on the effect of zeolite structure on the catalytic performance of Fe/zeolites in N_2O abatement.

It has been reported that isolated cationic iron species, di- and oligo-meric iron species, oligonuclear Fe-O-Al mixed oxides, and large iron oxide nanoparticles on the external surface of the zeolite are all potentially active sites for N_2O decomposition [14]. The structure of the active sites is related to the specific synthesis and activation procedures and/or to a particular confinement of the iron species imposed by the microporous structure of the zeolite. Wicherlová's group [15–19] suggested that Co(II) ions mainly occupy three main cationic sites, α, β, and γ, in high-silica pentasil ring zeolites (FER, MFI, BEA, and MOR), based on Fourier-transform infrared (FT-IR) and ultraviolet-visible (UV-Vis) diffuse reflectance spectroscopy using Co(II) ions as a probe. The suggested locations of the Co(II) ions in α, β, and γ sites in high-silica pentasil ring zeolites are further supported by the identification of Cu(II) ions at α cationic framework sites in mordenite [20] and of Ni(II) ions at β cationic framework sites in Ni-ferrierite [21]; these results were obtained using single-crystal X-ray diffraction and synchrotron powered X-ray diffraction, respectively. The spatial arrangement of divalent transition-metal ions in pentasil ring zeolites is therefore universal.

The structures of the active iron sites in Fe/zeolites, particularly Fe/ZSM-5 and Fe/ZSM-35, have been studied by Li's Group [22,23]. It is found that binuclear iron sites are the active sites for N_2O decomposition in Fe/ZSM-5 and Fe/ZSM-35. In this work, a combination of various spectroscopic techniques was used to investigate the catalytic properties of Fe-containing zeolites with different structures in N_2O decomposition.

2. Experimental

2.1. Catalyst preparation

Fe/zeolites samples with Fe/Al molar ratios of 0.33 were prepared using a solid-state ion-exchange method. NH_4^+/zeolite (2 g) was calcined at 823 K for 2 h in flowing helium. The reactor was then cooled to room temperature, sealed, and placed in a glove box. The reactor was opened in the glove box, and the resulting H/zeolite was removed and ground with an appropriate amount of anhydrous $FeCl_3$ (Sigma-Aldrich, AR) in a mortar. The mixture was returned to the reactor, and the reactor was resealed and removed from the glove box. The reactor was heated to 598 K and kept at this temperature for 2 h. The resulting solid was treated in a flow of 0.5% H_2O in helium from room temperature to 498 K to hydrolyze the Fe–Cl bonds. Finally, the sample was calcined at 823 K for 2 h in a flow of oxygen; the sample was denoted Fe/zeolite-C, where C refers to calcination in O_2. A fraction of Fe/zeolite was further treated at 1173 K for 2 h in flowing helium to obtain Fe/zeolite-HT, where HT denotes high-temperature treatment. NH_4^+/ZSM-5 (SiO_2/Al_2O_3 = 25), NH_4^+/beta (SiO_2/Al_2O_3 = 26), NH_4^+/ZSM-35 (SiO_2/Al_2O_3 = 21), and NH_4^+/mordenite (SiO_2/Al_2O_3 = 23) were used.

2.2. Catalyst characterization

The chemical compositions of the catalysts were determined using inductively coupled plasma-atomic emission spectrometry.

X-ray diffraction (XRD) data were collected using a Rigaku D/MAX 2500 diffractometer (40 kV, 200 mA, Cu K_α radiation). The step size was 0.02° and the scan speed was 5°/min.

UV-Vis diffuse reflectance spectra were collected at room temperature using a JASCO V-550 UV-visible spectrometer ($BaSO_4$ was used as a reference). Deconvolution of the UV-visible absorbance bands into Gaussian sub-bands, followed by multiplying the percentage of sub-bands with respect to the total area of the experimental spectrum with the total iron content, gives the percentage of different Fe species in the Fe/zeolites-C samples [12]. This quantification method does not account for the dependences of the extinction coefficients of various iron species on the wavelength but nevertheless provides a semi-quantitative estimation of the distributions of the various Fe species.

FT-IR spectra were recorded using a Nicolet Impact FT-IR spectrometer with a mercury cadmium telluride detector in transmission mode at a resolution of 4 cm^{-1}. The Fe/zeolites samples were pressed into self-supporting wafers (ca. 10 mg/m^2) and placed in a quartz IR cell with two CaF_2 windows. The Fe/zeolites-C samples were pretreated at 623 K for 1 h in flowing O_2, and the Fe/zeolites-HT samples were pretreated in a helium flow for 1 h. A reference spectrum was recorded. The samples were then cooled to room temperature in the same gas flow. The in-situ pretreated samples were exposed to 1.0% NO/He and then purged with helium. The gas flow rate was 60 ml/min. The intensity of each IR spectrum was normalized at the overtones of the zeolite lattice (1500–2000 cm^{-1}).

Visible Raman spectra were recorded in situ on a laboratory-made triple-stage Raman spectrometer with an excitation laser line at 532 nm emitted from a semiconductor laser. The sample was pressed into a self-supporting wafer and placed in an in-situ quartz cell. The sample was first calcined in O_2 at 823 K for 1 h, followed by treatment in helium at 1173 K for 1 h. A flow of 5.0% N_2O/He was then introduced into the quartz cell. After each treatment, the sample was cooled to room temperature to record the Raman spectrum.

A transient response method was used to measure the concentrations of active iron sites. The Fe/zeolites-C samples were pretreated in O_2 at 823 K for 1 h, and the Fe/zeolites-HT samples were pretreated in helium at 1173 K for 1 h. The sample was then cooled in flowing helium to the temperature of the transient response experiment. The tail gas was continuously monitored in the reactor outlet after switching from a helium flow to a 5.0% N_2O/He flow. The quantity of active Fe(II) sites was calculated by integration of the N_2 evolved.

2.3. *Activity measurements*

Catalytic decomposition of N_2O over the Fe/zeolites-C/HT catalysts was carried out in a U-shaped quartz reactor with an inner diameter of 4 mm. About 50 mg of catalyst were placed between two quartz-wool plugs; the gas mixture was 5.0% N_2O/He at a gas head space velocity of 24 000 h^{-1}. An on-line mass spectrometer (Gam 200, Pfeiffer Vacuum) was used for quantitative analysis of tail gas compositions.

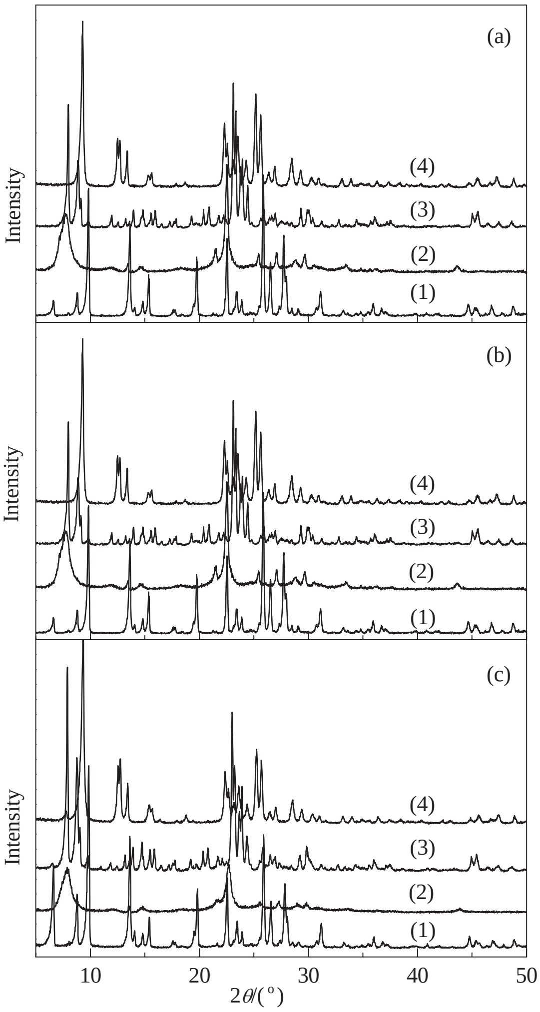

Fig. 1. XRD patterns of H/zeolites (a), Fe/zeolites-C (b), and Fe/zeolites-HT (c) samples. (1) H(Fe)/mordenite; (2) H(Fe)/beta; (3) H(Fe)/ZSM-35; (4) H(Fe)/ZSM-5.

3. Results and discussion

3.1. *Characterization of H(Fe)/zeolites*

Figure 1(a) presents the XRD patterns of the H/mordenite, H/beta, H/ZSM-35, and H/ZSM-5 zeolites. The expected diffraction patterns for the various zeolite structures and good crystallinities are observed for all the H/zeolites. For the Fe/zeolites-C/HT samples, only XRD reflections assigned to zeolite frameworks are observed, and no XRD patterns ascribed to iron oxide nanoparticles appear (Fig. 1(a) and (c)). This indicates that the long-range order of the zeolite frameworks is not affected, and high dispersion of iron species on the zeolites is obtained.

3.2. *UV-visible diffuse reflectance spectra of Fe/zeolites*

The coordination environments of various Fe species in Fe/zeolites-C/HT samples were characterized using UV-Vis diffuse reflectance spectroscopy. Figure 2(a) displays the UV-Vis diffuse reflectance spectra of Fe/zeolites-C samples. The UV-Vis diffuse reflectance spectrum of Fe/mordenite-C shows three intense Fe(III) ← O charge-transfer (CT) bands at 240, 275, and 360 nm, as well as a very weak shoulder at 540 nm. For the Fe/beta-C and Fe/ZSM-5-C samples, two intense ligand-to-metal CT bands at 240 and 360 nm and a smaller contribution at 540 nm appear. The Fe/ZSM-35-C sample also exhibits absorption bands at 240, 275, 360, and 540 nm, and the

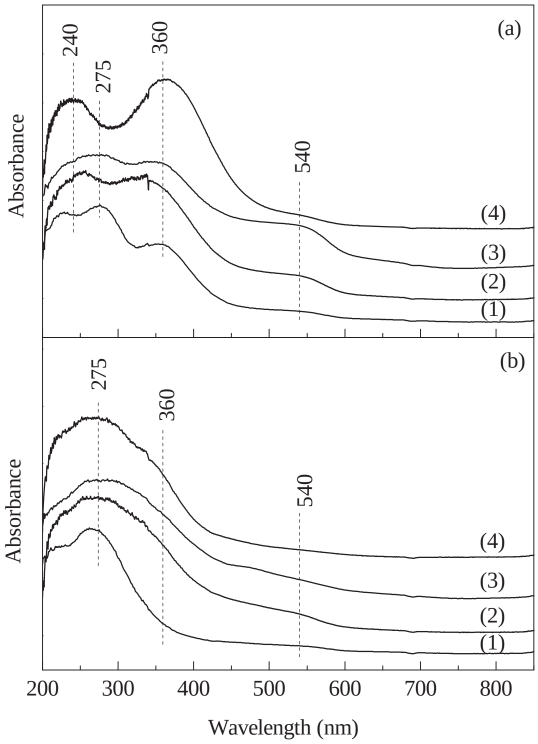

Fig. 2. UV-Vis diffuse reflectance spectra of Fe/zeolites-C (a) and Fe/zeolites-HT (b) samples. (1) Fe/mordenite; (2) Fe/beta; (3) Fe/ZSM-35; (4) Fe/ZSM-5.

Table 1
Percentage of the area of sub-bands (I_1 at $\lambda < 300$ nm, I_2 at $300 < \lambda < 400$ nm, I_3 at $\lambda > 400$ nm) of UV-visible diffuse reflectance spectra (Fig. 2(a)) and corresponding Fe mass percentage derived from total Fe content in Fe/zeolites-C.

Catalyst	Fe[a]	Fe[b]		Fe[c]		Fe[d]	
	w/%	I_1	*w*/%	I_2	*w*/%	I_3	*w*/%
Fe/mordenite-C	1.0	54	0.55	33	0.33	13	0.13
Fe/ZSM-5-C	1.1	32	0.38	64	0.77	4	0.05
Fe/beta-C	1.1	23	0.28	65	0.78	12	0.14
Fe/ZSM-35-C	1.5	49	0.74	24	0.36	27	0.40

[a] Determined by ICP. [b] Isolated Fe ions in tetrahedral and octahedral coordination. [c] Oligo-nuclear Fe_xO_y clusters ($x \geq 2$). [d] Bulk Fe oxides.

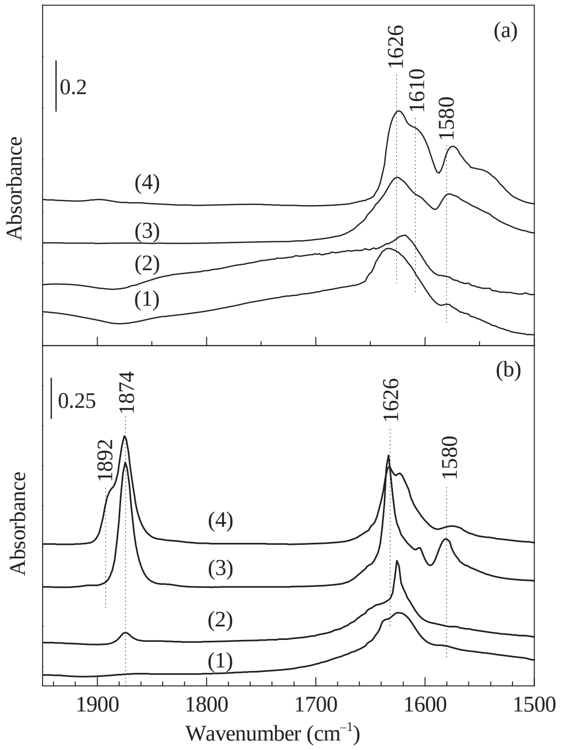

Fig. 3. FT-IR spectra of adsorbed NO on Fe/zeolites-C (a) and Fe/zeolites-HT (b) samples. (1) Fe/mordenite; (2) Fe/beta; (3) Fe/ZSM-35; (4) Fe/ZSM-5.

intensity of the absorption band at 540 nm is significantly higher than those of the other three Fe/zeolites-C samples. Figure 2(b) presents the UV-Vis diffuse reflectance spectra of the Fe/zeolites-HT samples. The intensity of the CT band at 275 nm is higher, whereas those of the absorption bands centered at about 240, 360, and 540 nm are lower than those in the Fe/zeolites-C samples, indicating that high-temperature treatment induces significant changes in iron speciation in all the Fe/zeolites samples.

In the literature, the CT bands between 200 and 300 nm are typically assigned to isolated Fe species with tetrahedral or higher coordinations [24–27], the broad bands between 300 and 450 nm are assigned to small oligomeric Fe_xO_y clusters, and the bands above 450 nm are assigned to large iron oxide aggregates [28]. We therefore ascribe the absorption bands at 240 and 275 nm to Fe(III) ← O CT of tetrahedrally coordinated Fe ions and octahedrally coordinated Fe ions, respectively. The band at 360 nm is related to oligonuclear Fe species, and the band at about 540 nm arises from bulky iron oxide nanoparticles. On high-temperature activation, the amount of isolated iron species in octahedral coordination increases, and the quantity of oligomeric iron clusters and large Fe_xO_y particles decreases. The relative amounts of different iron species are listed in Table 1. The relative quantities of isolated and oligomeric Fe species in the Fe/zeolites-C samples are in the order Fe/ZSM-35-C > Fe/ZSM-5-C > Fe/beta-C > Fe/mordenite-C, suggesting that iron species are present mainly as isolated and oligonuclear cationic species in the zeolite micropores or on the external surface of the zeolite.

3.3. *IR spectra of NO adsorption on Fe/zeolites samples*

Figure 3(a) and (b) shows the IR spectra in the region 1500–1900 cm^{-1} after exposure of the Fe/zeolites-C/HT samples to NO for 30 min and then purging in a flow of helium. An IR band at 1626 cm^{-1} with shoulder bands at 1610 and 1580 cm^{-1} can be observed for the Fe/zeolites-C samples. Significant changes take place in the IR spectra of the catalysts treated in helium at 1173 K. Besides the IR band at 1626 cm^{-1} with a shoulder band at 1580 cm^{-1}, a new characteristic IR band at 1874 cm^{-1} appears. For the Fe/ZSM-5-HT catalyst, another IR band at 1892 cm^{-1} is observed. Based on the literature data, the bands at 1580, 1610, and 1626 cm^{-1} are assigned to monodentate/bidentate nitro or nitrate species adsorbed on iron oxide species [29–31]. One explanation for the appearance of the nitro and nitrate species could be that some oxidation of NO by residual oxygen or extra-framework oxygen to N_2O_4, NO_2, NO^{3-}, or NO^{2-} occurs, or very small amounts of NO_2 are present in the NO probe gas. The strong IR band at 1874 cm^{-1} arises from NO adsorbed on Fe cations of the extra-framework Fe–O–Al oxide clusters [22], and the shoulder band at 1892 cm^{-1} is ascribed to mononitrosyl species formed on isolated or oligonuclear iron species [32]. These two IR bands correspond to the adsorption of NO on Fe(II) sites, not on Fe(III) sites [33]. From the results presented above, it appears that the cationic iron species that initially compensate for the negative framework charge of the Al-occupied oxygen tetrahedra are partially transformed into extra-framework Fe–O–Al oxide clusters upon high temperature treatment; this is very important for N_2O decomposition [22].

3.4. *Visible Raman spectra of Fe/zeolites samples*

Visible resonance Raman spectroscopy has proven to be a very powerful tool for the identification of the active oxygen species in Fe/zeolites, such as $Fe_2(\mu\text{-}1,2\text{-}O_2)$ species in Fe/ZSM-5 and $Fe_2(\mu\text{-}O)_2$ species in Fe/ZSM-35 [23,34]. Tuning a laser near or into the characteristic absorption feature of the sample leads to in-resonance or resonance enhancement of Raman bands associated only with this chromophore, the intensity of which can be increased as much as 10^4–10^6 fold compared with normal Raman scattering [35,36]. Figure 4(a) shows the visible Raman spectra, excited at 532 nm, of the

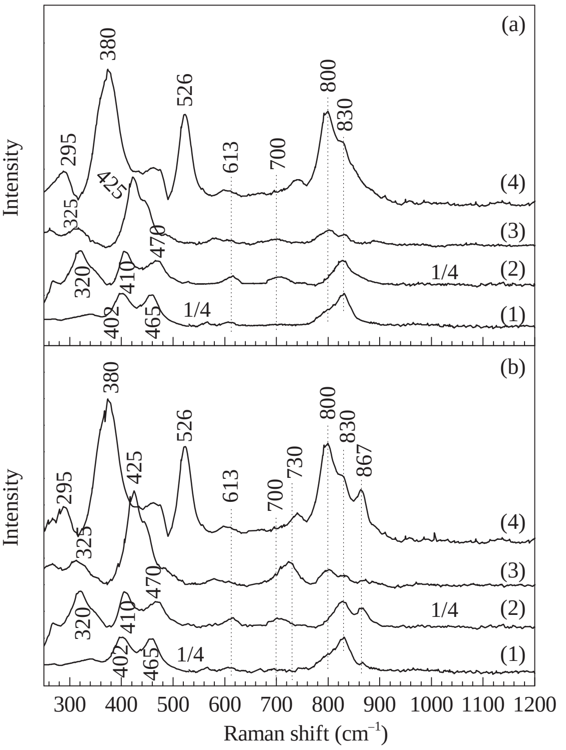

Fig. 4. Visible Raman spectra recorded in situ of Fe/zeolites-HT samples (a) and after exposure of (a) to 5.0% N_2O/He at 523 K (b). (1) Fe/mordenite-HT; (2) Fe/beta-HT; (3) Fe/ZSM-35-HT; (4) Fe/ZSM-5-HT. The excitation laser line: 532 nm.

Fe/zeolites-HT samples. The Raman spectrum of Fe/mordenite-HT has bands centered at 402, 465, 800, and 830 cm^{-1}, which are the characteristic bands of the MOR structure [37–39]. The Raman spectrum of the Fe/beta-HT presents new bands at 320, 410, 470, 613, 700, and 830 cm^{-1}. The Raman bands at 320, 410, and 470 cm^{-1} are assigned to bending modes of five-membered, six-membered, and four-membered rings, respectively [40]. The band at 830 cm^{-1} is often associated with symmetric stretching vibrations of Si–O bonds [41]. The bands at 613 and 700 cm^{-1} probably correspond to some iron oxides and oxyhydroxides [42], or to the Si–O bonds of a non-crystalline Si–O matrix surrounding the domains of the BEA structure [43,44]. The spectrum of Fe/ZSM-35-HT has bands at 325, 425, 800, and 830 cm^{-1}, which are characteristic of the ZSM-35 framework [43,45–48]. For Fe/ZSM-5-HT, in addition to the characteristic bands of the MFI structure at 295, 380, 460, and 800 cm^{-1}, a new band at 526 cm^{-1} is observed. This band is attributed to symmetric stretching vibrations of an Fe–O–Fe cluster of low nuclearity [22,49]. After exposure of the Fe/zeolites-HT samples to 5.0% N_2O/He at 523 K, Fe/mordenite-HT, Fe/beta-HT, and Fe/ZSM-5-HT exhibit a new Raman band at 867 cm^{-1}, and Fe/ZSM-35-HT shows a new Raman band at 730 cm^{-1} (Fig. 4(b)). The Raman bands at 867 and 730 cm^{-1} are attributed to peroxide species bridging binuclear Fe sites [34] and symmetric stretching vibrations of binuclear $Fe_2(\mu\text{-}O)$ sites, respectively [23]. Almost no Raman band corresponding to binuclear Fe sites can be observed in the spectrum of Fe/mordenite-HT.

3.5. *Concentrations of active Fe sites in Fe/zeolites samples*

The concentrations of active Fe sites were determined using a transient response method. Fig. 5(a) shows the product–time profiles in the reactor outlet after switching from a helium flow to a 5.0% N_2O/He flow for the Fe/ZSM-5-HT sample. Only N_2 and N_2O appear in the outlet, indicating the formation of surface oxygen atoms during N_2O decomposition at low temperature. Similar experiments using the Fe/zeolites-C samples revealed that the amount of N_2 evolved was negligible, suggesting that high-temperature activation is a prerequisite for the formation of active Fe sites [22]. The concentration of active Fe sites per gram of a Fe/zeolite-HT sample can be obtained by integrating the peak of the N_2 released; the results are listed in Table 2. The concentrations of active Fe sites in the Fe/zeolites-HT samples are in the order Fe/ZSM-35-HT > Fe/beta-HT > Fe/ZSM-5-HT > Fe/mordenite-HT; this is in agreement with the FT-IR spectra. The intensity of the IR band at 1874 cm^{-1} has a proportional linear relation with the concentration of active iron sites (Fig. 5(b)). The FT-IR and visible Raman spectra, combined with the transient response experimental results, indicate that binuclear iron sites stabilized by

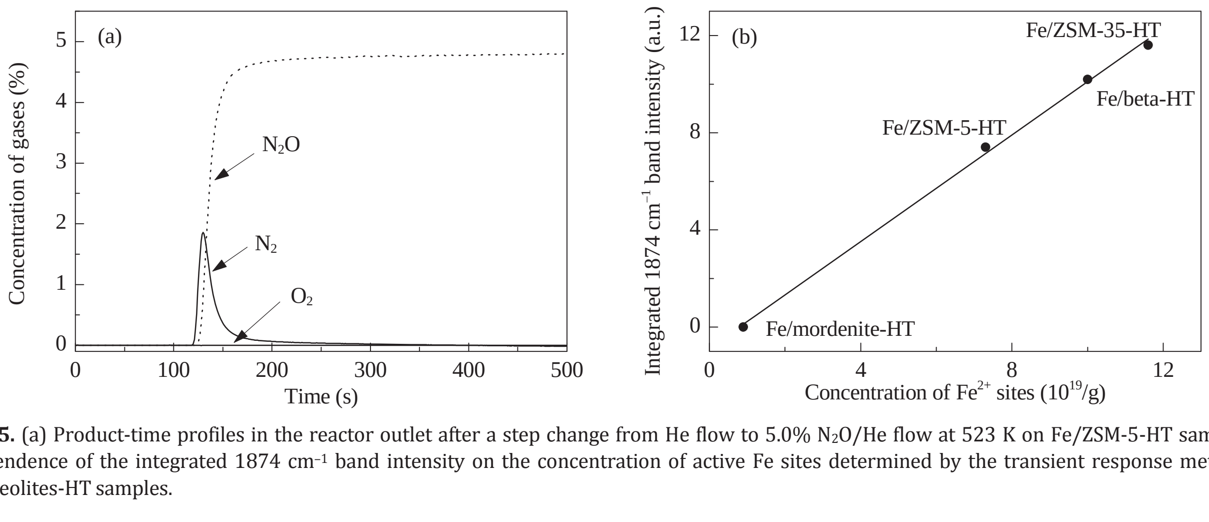

Fig. 5. (a) Product-time profiles in the reactor outlet after a step change from He flow to 5.0% N_2O/He flow at 523 K on Fe/ZSM-5-HT sample; (b) Dependence of the integrated 1874 cm^{-1} band intensity on the concentration of active Fe sites determined by the transient response method for Fe/zeolites-HT samples.

Table 2
Concentration of active Fe sites determined by the transient response method and the reaction rate of N_2O decomposition over Fe/zeolites-C/HT samples.

Catalyst	N_2O decomposition [active Fe sites] (10^{19}/g)	$R(N_2O)^{a}$/ (mmol/(g·h))	$R(N_2O)^{b}$/ (mmol/(g·h))
Fe/mordenite	0.9	0.7	1.1^{b}
Fe/ZSM-5	7.3	10.4	15.0^{b}
Fe/beta	10.0	6.6	17.6^{b}
Fe/ZSM-35	11.6	15.4	19.1^{c}

[a] Rate of N_2O decomposition at 733 K for Fe/zeolites-C samples.
[b] Rate of N_2O decomposition at 713 K for Fe/mordenite-HT, Fe/beta-HT, and Fe/ZSM-5-HT samples.
[c] Rate of N_2O decomposition at 673 K for Fe/ZSM-35-HT sample.

extra-framework Al in Fe/ZSM-35-HT, Fe/ZSM-5-HT, and Fe/beta-HT samples are the active sites in N_2O decomposition. Only a very small amount of N_2 was released in the transient response experiments, suggesting that almost no binuclear Fe sites are formed in the Fe/mordenite-HT sample.

3.6. *Catalytic activities of Fe/zeolites in N_2O decomposition*

Figure 6(a) shows the N_2O conversion versus temperature curves in N_2O decomposition for the Fe/zeolites-C catalysts. For the Fe/ZSM-35-C, Fe/ZSM-5-C, and Fe/beta-C catalysts, N_2O conversion starts at 700 K and is complete at about 773 K. For the Fe/mordenite-C catalyst, the reaction takes place at 743 K and finishes at 853 K. The rates of N_2O decomposition at 733 K for the Fe/zeolites-C catalysts are in the order Fe/ZSM-35-C > Fe/ZSM-5-C > Fe/beta-C > Fe/mordenite-C (Table 2). Clearly, the rate of N_2O decomposition increases linearly with the total quantity of isolated and oligonuclear Fe species (Fig. 7(a)), indicating that various types of Fe species, except large iron oxide nanoparticles, contribute to direct N_2O decomposition.

The catalytic activities of all the Fe/zeolites catalysts in N_2O decomposition increased significantly upon high-temperature treatment. The required temperature for 50% N_2O conversion over the Fe/zeolites-HT samples was reduced by 80 K for Fe/ZSM-35-HT, 50 K for Fe/beta-HT, 40 K for Fe/ZSM-5-HT, and 30 K for Fe/mordenite-HT compared with their corresponding calcined counterparts (Fig. 6). The N_2O conversions at 713 K for the Fe/zeolites-HT catalysts are in the order Fe/ZSM-35-HT > Fe/beta-HT > Fe/ZSM-5-HT > Fe/mordenite-HT. Moreover, the rate of N_2O decomposition at 713 K for the Fe/zeolites-HT catalysts is directly proportional to the concentration of active binuclear Fe sites, suggesting that the active binuclear Fe sites bound to extra-framework Al are responsible for direct N_2O decomposition (Fig. 7(b)). The catalytic properties of the Fe/mordenite-C and Fe/mordenite-HT catalysts in N_2O decomposition are very similar, indicating a low concentration of active binuclear Fe sites.

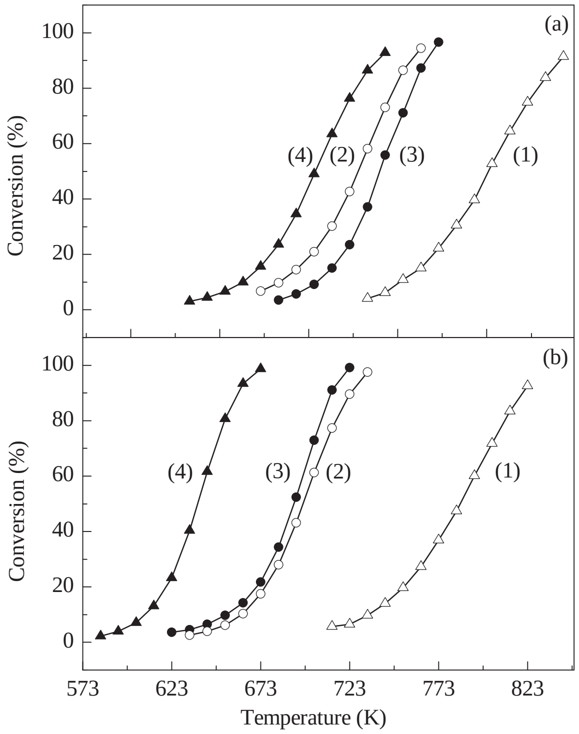

Fig. 6. N_2O conversion versus temperature over Fe/zeolites-C (a) and Fe/zeolites-HT (b) samples. (1) Fe/mordenite; (2) Fe/ZSM-5; (3) Fe/beta; (4) Fe/ZSM-35. Reaction conditions: 5.0% N_2O/He.

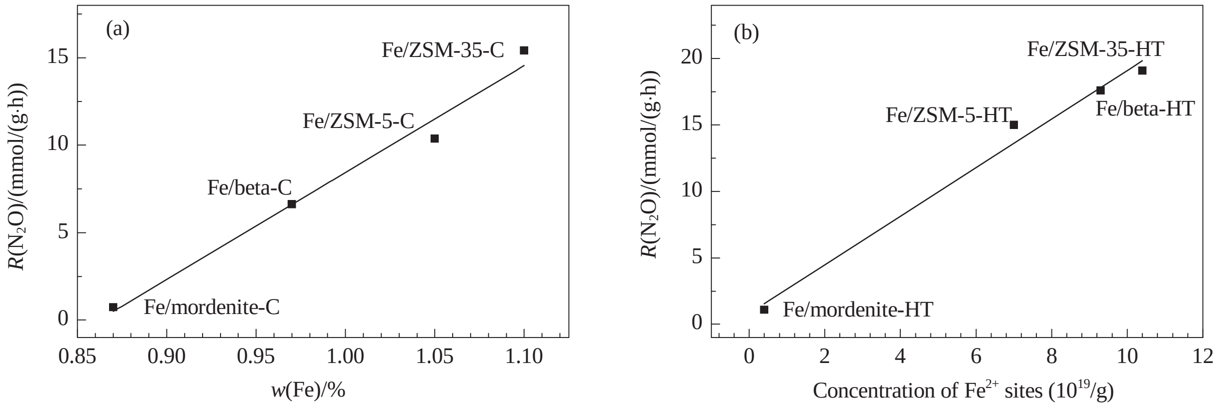

Fig. 7. (a) Dependence of the rate of N_2O decomposition at 733 K on the total amount of isolated iron ions, bi-nuclear, and oligo-nuclear iron clusters estimated from the UV-Vis diffuse reflectance spectra of Fe/zeolites-C samples; (b) Dependence of the rate of N_2O decomposition at 713 K on the concentration of Fe(II) sites determined by the transient response method for Fe/zeolites-HT samples. For the Fe/ZSM-35-HT sample, the rate of N_2O decomposition was calculated at 673 K.

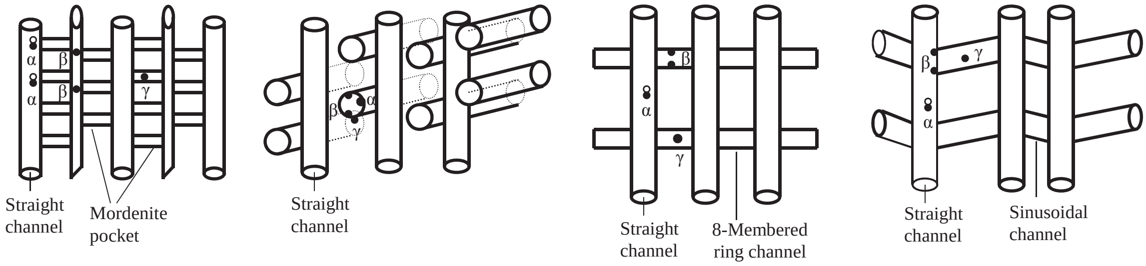

Mordenite Beta ZSM-35 ZSM-5

Fig. 8. The α-, β-, and γ-type cationic sites in mordenite, beta, ZSM-35, and ZSM-5 zeolites.

The differences among the catalytic activities of the Fe/zeolites-HT samples are associated with differences in the concentrations of active binuclear Fe sites. Furthermore, the formation of active binuclear Fe sites correlates well with the zeolite framework type. For Fe/zeolites catalysts prepared using an ion-exchange method, three main cationic positions, α, β, and γ, are populated by divalent cations in high-silica zeolites [9]. Figure 8 displays the α-, β-, and γ-type cationic sites in FER, MFI, BEA, and MOR structures. The α-type site is a six-membered ring composed of two five-membered rings (5-MR) and located in the main channels of the MOR, FER, and MFI frameworks or in the cages of polymorph C of the BEA framework. The β-type site is a twisted eight-membered ring (8-MR) in the MOR cavity, or a deformed six-membered ring (6-MR) located in the FER cavity, whereas in the ZSM-5 and beta zeolites, the β-type site is related to a deformed six-membered ring at the intersection of the straight and sinusoidal channels of ZSM-5 or inside the cages of polymorphs A and B of beta zeolite. The γ-type site corresponds to a boat-shaped site in the FER, MFI, and MOR frameworks, or a position inside the cages of polymorphs A and B of the beta zeolite.

The different frameworks have an impact on the accessibility of Co(II) ions located in the individual sites of zeolites. Dědeček et al. [50,51] reported that only Co(II) cations accommodated in the α and β sites of zeolites are accessible to reactants and can play a role as reaction centers, whereas γ-type Co(II) cations are not accessible to reactants in Co/zeolite samples. Moreover, it is generally accepted that O_2 desorption is the rate-determining step for N_2O decomposition [25]. Short distances between the active Fe sites might therefore increase the probability of combination and desorption of adsorbed oxygen atoms. The distances between the two closest cationic sites represent the distances between the two closest cations. Different zeolite structures result in different distances of the two Fe(II) cations accommodated in two adjacent collaborating α or β sites in ZSM-35, beta, ZSM-5, and mordenite. The distances between the neighboring α and β sites in FER are 0.54 and 0.61 nm, respectively, and those between two adjacent β sites in beta, ZSM-5, and mordenite are 0.75, 0.45, and 0.7 nm, respectively [50]. The distance between two neighboring α sites in ZSM-5 is 0.75 nm, but the sites do not face each other, indicating that they are possibly not favorable for N_2O decomposition. The distance between two neighboring β sites is 0.75 nm, and their appropriate arrangement is beneficial for the formation of the transition state in N_2O decomposition [8,10]. Two adjacent collaborating α or β sites in the main channel of the ZSM-35 zeolite, two neighboring β sites inside the cages of polymorphs A and B of the beta zeolite, and two β sites at the intersection of the straight and sinusoidal channels of the ZSM-5 structure are therefore appropriate for the formation of active binuclear Fe sites favorable for N_2O decomposition.

Other important parameters controlling the formation of active Fe sites are the distributions and concentrations of Al pairs in specific cationic sites of high-silica zeolites; these have been shown to control the structures and concentrations of Fe ions in these zeolites [10,52]. The formation of binuclear Fe sites requires the presence of two Al atoms in each of the two cooperating cationic sites. The upper limit of the probability of the presence of an Al pair in each ring of the specific cationic sites can be estimated using bare Co(II) ions as a probe, analyzed by UV-visible diffuse reflectance absorbance spectroscopy [15–19].

Sklenak et al. [10] showed that the maximum loading of bare Co(II) ions is Co/Al = 0.31 in ZSM-35 zeolite. Thus, 62% of all framework Al atoms are accommodated as pairs in the six-membered rings of α and β sites. The Si/Al ratio of the ZSM-35 sample is 10.5, meaning that the concentration of Al atoms is 7.9×10^{-4} mol/g. The Fe exchange at Fe/Al = 0.33 corresponds to 4.9×10^{-4} mol of Al atoms per gram of Fe/ZSM-35 sample ($7.9 \times 10^{-4} \times 0.62$). According to the literature, about 5% and 85% of Fe(II) cations are located at α- and β-type cationic sites, respectively [18]. The concentration of Fe(II) ions located in two adjacent collaborating α and β sites that are able to form binuclear Fe sites is therefore 2.5×10^{-4} mol/g. The maximum Co/Al ratio reached for Co(II) ions exchanged to beta (Si/Al = 13) was 0.45, showing that 90% of framework Al atoms are located in 6-MR as Al pairs. Among these, 55% of the Co(II) ions are located at β sites [17]. The Fe/Al ratio of 0.33 of the Fe/beta catalyst means that the concentration of Al pairs at β sites is 3.2×10^{-4} mol/g and the concentration of binuclear Fe sites is 1.6×10^{-4} mol/g. For the ZSM-5 sample investigated, the maximum Co/Al ratio was 0.4, suggesting that 80% of the framework Al atoms are distributed in 6-MR as Al–O–Si–O–Al pairs, of which 50% occupy β-type cationic sites [53]. This indicates that 40% of the framework Al atoms are accommodated in the six-membered rings of cationic β sites. The highest attainable loading of Fe(II) ions at cationic β sites (Fe/Al = 0.33) in ZSM-5 (Si/Al = 12.5) is therefore 1.3×10^{-4} mol/g. In summary, the concentrations of active binuclear Fe sites in the

Fe/ZSM-35-HT, Fe/beta-HT, and Fe/ZSM-5-HT samples are in the order Fe/ZSM-35-HT > Fe/beta-HT > Fe/ZSM-5-HT. This is in agreement with the catalytic performance of the Fe/zeolites-HT samples in direct N_2O decomposition.

4. Conclusions

The effect of zeolite structure on the catalytic performance of Fe/zeolites-HT samples in N_2O decomposition was investigated using UV-visible diffuse reflectance, in-situ FT-IR, and in-situ visible Raman spectroscopic techniques in combination with a transient response method. The catalytic activities of the Fe/zeolites-HT samples were in the order Fe/ZSM-35-HT > Fe/beta-HT > Fe/ZSM-5-HT > Fe/mordenite-HT. A good relationship was found between the rate of N_2O decomposition and the concentration of binuclear Fe sites, indicating that the binuclear Fe sites are the active sites for N_2O decomposition. It was shown that two Fe(II) cations located in two adjacent collaborating six-membered rings in a 10-membered ring channel (α sites) or in two adjacent six-membered rings in an eight-membered ring channel (β sites) in the ZSM-35 framework can form active binuclear iron sites. Similar structures can also be formed in two adjacent six-membered rings in polymorphs A and B of the beta zeolite or in two neighboring six-membered rings at the intersection of straight and sinusoidal channels of the ZSM-5 zeolite.

References

[1] Pérez-Ramírez J, Kapteijn F, Schöffel K, Moulijn J A. *Appl Catal B*, 2003, 44: 117
[2] Pérez-Ramírez J, Kapteijn F, Mul G, Xu X, Moulijn J A. *Catal Today*, 2002, 76: 55
[3] Parmon V N, Panov G I, Uriarte A, Noskov A S. *Catal Today*, 2005, 100: 115
[4] Hansen N, Heyden A, Bell A T, Keil F J. *J Catal*, 2007, 248: 213
[5] Pirngruber G D, Roy P K, Prins R. *J Catal*, 2007, 246: 147
[6] Roy P K, Prins R, Pirngruber G D. *Appl Catal B*, 2008, 80: 226
[7] Øygarden A H, Pérez-Ramírez J. *Appl Catal B*, 2006, 65: 163
[8] Kaucký D, Sobalík Z, Schwarze M, Vondrová A, Wichterlová B. *J Catal*, 2006, 238: 293
[9] Jíša K, Nováková J, Schwarze M, Vondrová A, Sklenák S, Sobalik Z. *J Catal*, 2009, 262: 27
[10] Sklenák S, Andrikopoulos P C, Boekfa B, Jansang B, Nováková J, Benco L, Bucko T, Hafner J, Dědeček J, Sobalík Z. *J Catal*, 2010, 272: 262
[11] Pantu P, Boekfa B, Sunpetch B, Limtrakul J. *Chem Eng Commun*, 2008, 195: 1477
[12] Pérez-Ramírez J, Groen J C, Brückner A, Kumar M S, Bentrup U, Debbagh M N, Villaescusa L A. *J Catal*, 2005, 232: 318
[13] Melián-Cabrera I, Mentruit C, Pieterse J A Z, van den Brink R W, Mul G, Kapteijn F, Moulijn J A. *Catal Commun*, 2005, 6: 301
[14] Xia H A, Sun K Q, Fan F T, Sun K J, Su W G, Feng Zh Ch, Ying P L, Li C. *J Catal*, 2008, 259: 269
[15] Dědeček J, Kaucký D, Wichterlová B. *Microporous Mesoporous Mater*, 2000, 35-36: 483
[16] Sobalík Z, Dědeček J, Kaucký D, Wichterlová B, Drozdová L, Prins R. *J Catal*, 2000, 194: 330
[17] Dědeček J, Čapek L, Kaucký D, Sobalík Z, Wichterlová B. *J Catal*, 2002, 211: 198
[18] Drozdová L, Prins R, Dědeček J, Sobalík Z, Wichterlová B. *J Phys Chem B*, 2002, 106: 2240
[19] Dědeček J, Wichterlová B. *J Phys Chem B*, 1999, 103: 1462
[20] Attfield M P, Weigel S J, Cheetham A K. *J Catal*, 1997, 170: 227
[21] Dalconi M C, Cruciani G, Alberti A, Ciambelli P, Rapacciuolo M T. *Microporous Mesoporous Mater*, 2000, 39: 423
[22] Sun K Q, Xia H A, Feng Zh Ch, van Santen R, Hensen E J M, Li C. *J Catal*, 2008, 254: 383
[23] Wang J Y, Li G N, Ju X H, Xia H A, Fan F T, Wang J H, Feng Zh Ch, Li C. *J Catal*, 2013, 301: 77
[24] Kumar M S, Schwidder M, Grünert W, Brückner A. *J Catal*, 2004, 227: 384
[25] Pérez-Ramírez J. *J Catal*, 2004, 227: 512
[26] Pérez-Ramírez J, Kumar M S, Brückner A. *J Catal*, 2004, 223: 13
[27] Pérez-Ramírez J, Mul G, Kapteijn F, Moulijn J A, Overweg A R, Doménech A, Ribera A, Arends I W C E. *J Catal*, 2002, 207: 113
[28] Bordiga S, Buzzoni R, Geobaldo F, Lamberti C, Giamello E, Zecchina A, Leofanti G, Petrini G, Tozzola G, Vlaic G. *J Catal*, 1996, 158: 486
[29] Hadjiivanov K, Ivanova E, Kefirov R, Janas J, Plesniar A, Dzwigaj S, Che M. *Microporous Mesoporous Mater*, 2010, 131: 1
[30] Hensen E J M, Zhu Q, van Santen R A. *J Catal*, 2003, 220: 260
[31] Long J L, Zhang Z Zh, Ding Zh X, Ruan R Sh, Li Zh H, Wang X X. *J*

Graphical Abstract

Chin. J. Catal., 2013, 34: 876–888 doi: 10.1016/S1872-2067(12)60555-5

Catalytic performance of different types of iron zeolites in N_2O decomposition

WANG Junying, XIA Haian, JU Xiaohua, FAN Fengtao, FENG Zhaochi, LI Can*
Dalian Institute of Chemical Physics, Chinese Academy of Sciences;
Graduate University of Chinese Academy of Sciences

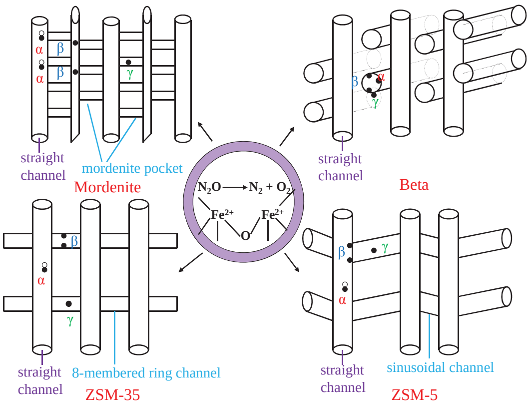

The influence of zeolite frameworks on the catalytic properties of Fe/zeolites in N_2O decomposition was investigated using a combination of UV-Vis diffuse reflectance, in-situ FT-IR, and in-situ visible Raman spectroscopic techniques with a transient response method.

Phys Chem C, 2010, 114: 15713
[32] Lobree L J, Hwang I-C, Reimer J A, Bell A T. *Catal Lett*, 1999, 63: 233
[33] Yuranov I, Bulushev D A, Renken A, Kiwi-Minsker L. *Appl Catal A*, 2007, 319: 128
[34] Xia H A, Sun K Q, Sun K J, Feng Zh Ch, Li W X, Li C. *J Phys Chem C*, 2008, 112: 9001
[35] Li C, Xiong G, Xin Q, Liu J K, Ying P L, Feng Zh Ch, Li J, Yang W B, Wang Y Zh, Wang G R, Liu X Y, Lin M, Wang X Q, Min E Z. *Angew Chem, Int Ed*, 1999, 38: 2220
[36] Fan F T, Xu Q, Xia H A, Sun K J, Feng Zh Ch, Li C. *Chin J Catal* (范峰滔, 徐倩, 夏海岸, 孙科举, 冯兆池, 李灿. 催化学报), 2009, 30: 717
[37] Nosheen S, Galasso F, Suib S L. *Sci Adv Mater*, 2009, 1: 31
[38] Twu J, Dutta P K, Kresge C T. *J Phys Chem*, 1991, 95: 5267
[39] Dutta P K, Rao K M, Park J Y. *J Phys Chem*, 1991, 95: 6654
[40] Fan F T, Feng Zh Ch, Li C. *Acc Chem Res*, 2010, 43: 378
[41] Yu Y, Xiong G, Li C, Xiao F-Sh. *Microporous Mesoporous Mater*, 2001, 46: 23
[42] de Faria D L A, Venaüncio Silva S, de Oliveira M T. *J Raman Spectrosc*, 1997, 28: 873
[43] Tosheva L, Mihailova B, Valtchev V, Sterte J. *Microporous Mesoporous Mater*, 2001, 48: 31
[44] Lewandowska A E, Banares M A, Tielens F, Che M, Dzwigaj S. *J Phys Chem C*, 2010, 114: 19771
[45] Dutta P K, Rao K M, Park J Y. *Langmuir*, 1992, 8: 722
[46] Suzuki Y, Wakihara T, Itabashi K, Ogura M, Okubo T. *Top Catal*, 2009, 52: 67
[47] Mihailova B, Valtchev V, Mintova S, Faust A-C, Petkov N, Bein T. *Phys Chem Chem Phys*, 2005, 7: 2756
[48] Majano G, Mintova S, Ovsitser O, Mihailova B, Bein T. *Microporous Mesoporous Mater*, 2005, 80: 227
[49] Fan F T, Sun K J, Feng Zh Ch, Xia H A, Han B, Lian Y X, Ying P L, Li C. *Chem Eur J*, 2009, 15: 3268
[50] Dědeček J, Kaucký D, Wichterlová B. *Top Catal*, 2002, 18: 283
[51] Kaucký D, Vondrová A, Dědeček J, Wichterlová B. *J Catal*, 2000, 194: 318
[52] Kapteijn F, Rodriguez-Mirasol J, Moulijn J A. *Appl Catal B*, 1996, 9: 25
[53] Dědeček J, Kaucký D, Wichterlová B, Gonsiorová O. *Phys Chem Chem Phys*, 2002, 4: 5406

不同类型含铁分子筛上N_2O催化分解反应

王俊英[a,b], 夏海岸[a], 鞠晓花[a], 范峰滔[a], 冯兆池[a], 李 灿[a,*]
[a]中国科学院大连化学物理研究所催化基础国家重点实验室, 辽宁大连116023
[b]中国科学院大学, 北京100049

摘要: 采用固态离子交换法制备了一系列Fe/Al摩尔比为0.33的Fe/分子筛(ZSM-35, ZSM-5, beta和mordenite (丝光沸石))样品, 并利用紫外-可见漫反射光谱、原位红外光谱和可见拉曼光谱以及瞬态应答实验考察了分子筛种类对N_2O分解反应性能的影响. 研究表明, 经高温处理(HT)后分子筛的催化活性顺序为 Fe/ZSM-35 > Fe/beta > Fe/ZSM-5 > Fe/mordenite, 与骨架外铝稳定的双核铁物种含量一致. 这说明双核铁物种是高温处理后Fe/分子筛样品中N_2O分解的活性位, 而它的形成与分子筛种类密切相关. Fe/ZSM-35分子筛十元环孔道中相邻两个α位和八元环孔道中相邻两个β位都能稳定两个Fe(II)离子而形成能高效分解N_2O的双核铁活性中心. Fe/beta和Fe/ZSM-5分子筛中只有落在相邻两个β位上的两个Fe(II)离子才能形成参与N_2O分解的高活性的双铁活性中心. Fe/mordenite-HT分子筛上的铁物种绝大部分以孤立Fe离子的形式存在, 因此其催化N_2O分解反应活性很低.

关键词: 铁; 分子筛; 氧化亚氮分解; 拉曼光谱

收稿日期: 2012-12-26. 接受日期: 2013-02-24. 出版日期: 2013-05-20.

*通讯联系人. 电话: (0411)84379070; 传真: (0411)84694447; 电子信箱: canli@dicp.ac.cn

基金来源: 国家自然科学基金(21173213); 国家重点基础研究发展计划(973计划, 2009CB623507).
本文的英文电子版由Elsevier出版社在ScienceDirect上出版(http://www.sciencedirect.com/science/journal/18722067).

1. 前言

含铁分子筛是一种优良的N_2O分解消除催化剂, 能将温室气体N_2O有效分解成N_2和O_2 [1,2]. Panov课题组 [3~6]发现, Fe/ZSM-5在N_2O分解反应中表现出独特而优异的催化性能. 然而, 到目前为止大部分有关含铁分子筛的工作都集中在Fe/ZSM-5体系上; 实验和理论的研究主要集中在催化剂的制备和预处理条件对Fe/ZSM-5活性位结构和性质的影响、N_2O消除反应的机理以及催化剂的实际应用等方面 [3~6]. 有关不同的含铁分子筛在N_2O消除反应中催化性能的研究 [7~13]较少.

Øygarden等 [7] 研究了含有1×10^{-6}级铁物种的商品化的BEA, FER和MFI分子筛在N_2O消除反应中的催化性能, 发现高温水蒸气处理后的BEA分子筛表现出最高的催化活性. 这可能是由于在高温水蒸气处理过程中, BEA分子筛骨架中的铁和铝更容易脱出骨架, 形成了骨架外铝稳定的双核或低聚的铁活性位造成的. Kaucký等 [8] 研究发现, 由于Fe/ferrierite中Fe-Fe之间的距离较短, 因而在N_2O消除反应中的催化性能比铁含量相似的Fe/beta更优异. Jíša等[9,10]通过实验与理论计算相结合的方式研究发现, 在Fe/ferrierite分子筛中存在一种特殊结构的铁活性位, 即八元环孔道中相邻两个六元环中的两

个Fe(II)离子, 从而使Fe/ferrierite分子筛在N_2O消除反应中表现出比Fe/ZSM-5和Fe/beta分子筛更优异的催化性能. Pantu等[11]研究发现, 在Fe/FER, Fe/BEA, Fe/ZSM-5和Fe/FAU四种分子筛中, 由于Fe/FER具有较小的孔道和较强的吸附N_2O的能力, 因而在N_2O消除反应中的催化活性最高. Pérez-Ramírez等[12]比较了Fe/MFI与Fe/BEA在N_2O消除反应中的催化性能, 认为不同的催化剂中存在结构类似的铁物种, 不同的微孔分子筛载体对催化剂的催化性能没有影响. Melián-Cabrera等[13]报道了Fe/FER在模拟硝酸工厂尾气条件下的N_2O消除反应中具有比Fe/MFI和Fe/BEA更优越的催化性能. 这可能是由于FER分子筛更有利于铁活性位的形成和稳定. 然而, 分子筛种类与含铁分子筛催化N_2O消除反应性能的关系尚不清楚.

研究认为, 不同的Fe/zeolites中, 骨架外孤立的铁阳离子、双核或低聚的铁物种、低聚的Fe-O-Al混合氧化物和分子筛外表面上较大的氧化铁纳米颗粒都可能是N_2O消除反应的活性中心[14]. 活性中心的结构与Fe/zeolites样品的制备方法、预处理条件以及铁物种在分子筛中的落位和配位环境密切相关. Wichterlová课题组[15~19]采用Co(II)离子为探针, 利用红外光谱(FT-IR)和紫外-可见漫反射(UV-Vis)光谱等研究发现, 在高硅的pentasil型分子筛(FER, MFI, BEA和MOR)中, Co(II)离子主要占据三种类型的阳离子位: α, β和γ位. Attfield等[20]和Dalconi等[21]分别利用单晶X射线衍射(XRD)和同步辐射的XRD技术研究了Cu-mordenite和Ni-ferrierite分子筛中Cu(II)离子和Ni(II)离子的落位. 他们发现, Cu(II)离子主要落在mordenite分子筛的α位上, Ni(II)离子主要落在ferrierite分子筛的β位上. 由此可知, 二价的过渡金属阳离子在pentasil型分子筛中的落位规律具有普适性.

近年来, 李灿课题组[22,23]对含铁分子筛, 特别是Fe/ZSM-5和Fe/ZSM-35在N_2O分解反应中的活性中心进行了深入的研究, 发现双核铁位是N_2O分解的活性中心. 本文综合运用多种谱学技术研究了几种Fe/zeolites (FER, MFI, BEA和MOR)在N_2O分解反应中的催化性能与分子筛结构的关系.

2. 实验部分

2.1. 催化剂的制备

采用固态离子交换法制备一系列Fe改性的ZSM-35, beta, ZSM-5和mordenite (丝光沸石)负载型催化剂, Fe/Al摩尔比为0.33. 典型的制备过程如下. 首先将2 g NH_4^+/zeolite在823 K下O_2中焙烧2 h, 接着将样品冷却到室温, 密封, 放入手套箱中. 在手套箱中, H/zeolite与适量的无水$FeCl_3$ (Sigma-Aldrich, AR)混合研磨. 研磨后的混合物重新放回反应器中, 再次将反应器密封, 取出手套箱. 在He气氛中, 样品的温度从室温升到598 K, 保持2 h. 温度降至498 K后, 在0.5% H_2O/He气氛中水解除去Fe–Cl键. 反应完成后, 将产物在823 K下O_2中焙烧2 h, 得到Fe/zeolite-C样品, C代表在823 K下O_2中焙烧(以下简称焙烧). 一部分Fe/zeolite-C样品在1173 K下He中处理2 h, 得到Fe/zeolite-HT样品, HT代表在1173 K下He中处理(以下简称高温处理). 所用四种分子筛载体分别是NH_4^+/ZSM-35 (SiO_2/Al_2O_3 = 21, 自制), NH_4^+/ZSM-5 (SiO_2/Al_2O_3 = 25), NH_4^+/beta (SiO_2/Al_2O_3 = 26)和NH_4^+/mordenite (SiO_2/Al_2O_3 = 23, 南开催化剂厂).

2.2. 催化剂的表征

样品化学组成由ICP-AES (电感耦合等离子体-原子发射光谱)测定. XRD谱在日本Rigaku D/MAX 2500型X射线衍射仪(40 kV, 200 mV, Cu K_α为射线源, 以0.02°间隔阶梯扫描, 扫描速度5°/min)上测定.

UV-Vis谱在室温下在JASCO V-550型紫外-可见光谱仪上测定(以$BaSO_4$作为参比样品). 将Fe/zeolite-C样品的紫外-可见漫反射光谱图用高斯函数作分峰拟合, 然后将各个拟合峰的相对强度与分子筛样品中的总铁含量相乘即得到Fe/zeolite-C样品中不同铁物种的含量[12]. 需要注意的是, 这种分析方法没有考虑各种铁物种在不同波长的吸收系数的差异.

样品的FT-IR谱在Nicolet Impact 470型红外光谱仪上采集. 采用液氮冷却的MCT-B探测器, 分辨率为4 cm^{-1}, 扫描次数为32次, 光谱扫描范围为4000~650 cm^{-1}. 具体过程如下. 将Fe/zeolite样品压成自支撑片(约10 mg/cm^2), 并放入以CaF_2为窗片的石英原位红外池中. Fe/zeolite-C样品在623 K下O_2中处理1 h, Fe/zeolite-HT样品在623 K下He中处理1 h. 接着将样品在相同的气氛中冷却到室温, 采集红外光谱作为相应样品的背景谱. 然后, 将原位处理的样品暴露在1.0% NO/He气氛中, NO吸附饱和后再用He吹扫10 min, 气体的流速均为60 ml/min. 每个样品的FT-IR谱峰强度用分子筛晶格振动的泛频区的谱峰强度(1500~2000 cm^{-1})作归一化.

样品的可见拉曼光谱在自主研制搭建的三光栅紫外-可见拉曼光谱仪上采集. 采用固态激光器发射的532 nm可见激光作光源. 首先将样品压成自支撑片, 放入石英原位反应池中. 再将样品在1173 K下He中处理1 h.

然后将样品冷却到523 K, 在石英原位反应池中通入5.0% N_2O/He混合气. 每次处理完成后, 将样品冷却到室温采集拉曼谱.

采用瞬态应答方法测定铁活性物种的量. 首先将Fe/zeolite-HT样品在1173 K下He中处理1 h, 然后冷却到瞬态应答反应所需要的温度. 再将气体换成5.0% N_2O/He混合气. 样品中铁活性物种的量通过计算生成N_2的积分面积获得.

2.3. 催化剂的评价

N_2O分解反应在直径为4 mm的U形石英反应器中进行, 催化剂用量50 mg. 原料气组成5.0% N_2O, He平衡气, GHSV为24000 h^{-1}. 尾气组成采用四级杆质谱仪(Gam 200, Pfeiffer Vaccum)在线检测.

3. 结果与讨论

3.1. H(Fe)/zeolite的XRD谱

图1(a)是H/mordenite, H/beta, H/ZSM-35和H/ZSM-5分子筛的XRD谱. 可以看出, 所用的H/zeolite载体有很好的结晶度, 担载了Fe之后, 无论是Fe/zeolite-C还是Fe/zeolite-HT样品都只观察到分子筛骨架的特征衍射峰, 且未观察到归属于氧化铁纳米颗粒的特征衍射峰(见图1(b)和(c)), 表明这些样品中分子筛的骨架得到了很好的保持, 并且Fe物种很好地分散于其上.

3.2. Fe/zeolite样品的紫外-可见漫反射光谱

采用UV-Vis谱表征了Fe/zeolite样品中各种铁物种的配位环境. 图2(a)为Fe/zeolite-C样品的紫外-可见漫反射光谱图. 由图可见, Fe/mordenite-C样品在240, 275和360 nm处出现吸收峰, 且在540 nm有一个弱的肩峰; Fe/beta-C和Fe/ZSM-5-C在240和360 nm处出现明显的吸收峰, 在540 nm出现一个弱的肩峰. 对于Fe/ZSM-35-C而言, 240, 275, 360和540 nm处吸收峰的强度比其它三种Fe/zeolite-C样品都要强. 图2(b)是Fe/zeolite-HT样品的紫外-可见漫反射光谱图. 可以看出, 高温处理后样品于275 nm处的吸收峰强度明显增大, 而240, 360和540 nm处的吸收峰强度明显减弱. 这表明高温处理使Fe/zeolite样品上的铁物种结构发生了显著的变化.

研究表明, 200~300 nm处吸收峰与四配位或更高配位的孤立铁物种的电荷转移跃迁有关[24~27], 300~450 nm处很宽的吸收峰归属于六配位或寡聚的铁物种, 450 nm以上的吸收峰则来自小的氧化铁纳米颗粒[28]. 因此, 240和275 nm处吸收峰分别与分子筛骨架中四配位的铁物种和分子筛骨架外六配位铁物种的O→Fe(III)的电荷转移跃迁有关; 360和540 nm处吸收峰则分别来自寡聚的铁物种和体相的氧化铁纳米颗粒. 由此可见, 高温处理后的样品中六配位的孤立铁物种明显增多, 同时寡聚的铁物种和氧化铁纳米颗粒的量显著减少. 用紫外-可见吸收光谱确定的不同铁物种的含量列于表1. 可以看出, Fe/zeolite-C样品中铁物种主要以孤立和寡聚的形式存在, 它们的总含量大小顺序为Fe/ZSM-35-C > Fe/ZSM-5-C > Fe/beta-C > Fe/mordenite-C. 这表明引入的Fe物种主要是以高分散的形式负载在分子筛的孔道中或外表面上.

3.3. Fe/zeolite样品的FT-IR谱

图3(a)和(b)分别为室温时1.0% NO在Fe/zeolite-C/HT样品上吸附饱和, 再经He吹扫后的原位FT-IR谱. 由图可见, Fe/zeolite-C样品分别在1626, 1610和1580 cm^{-1}处出现吸收峰, 经1173 K下He中处理后, 除1626和1580 cm^{-1}处吸收峰外, 还在1874 cm^{-1}处出现了一个新的吸收峰. 在Fe/ZSM-5-HT分子筛样品上还出现一个位于1892 cm^{-1}处的吸收峰. 1580, 1610和1626 cm^{-1}处吸收峰归属于铁氧化物上吸附的$–NO_3^-$和/或$–NO_2^-$基团的吸收振动峰[29~31]. 这可能是由于分子筛表面吸附的NO与反应气中残留的微量O_2或者分子筛表面的氧物种发生反应, 生成吸附态的N_2O_4, NO_2, NO_3^-或NO_2^-所致. 1874和1892 cm^{-1}处吸收峰则分别对应于骨架外Fe–O–Al物种[22]和孤立或寡聚的铁物种上NO的吸收振动峰[32]. 这两个峰均对应于NO在Fe(II)离子而不是Fe(III)离子上的吸附[33]. 综上可知, 高温处理过程中,骨架脱铝和铁物种结构的改变使得位于铝阳离子位的价键补偿铁离子转变成骨架外的Fe-O-Al混合氧化物, 后者在N_2O分解反应中起着重要的作用[22].

3.4. Fe/zeolite样品的可见拉曼光谱

李灿课题组[23,34]的研究表明, 可见共振拉曼光谱可以灵敏而高选择性地鉴定含铁分子筛中的活性氧物种, 比如Fe/ZSM-5分子筛中的$Fe_2(\mu\text{-}1,2\text{-}O_2)$物种和Fe/ZSM-35分子筛中的$Fe_2(\mu\text{-}O)_2$物种. 共振拉曼效应是指当采用的激光频率与待测分子的某个电子吸收峰接近或重合时, 这一分子的某个或几个特征拉曼谱带强度可以达到正常拉曼谱带的几倍甚至10^4~10^6倍[35,36]. 与正常拉曼光谱相比, 共振拉曼光谱在有特定吸收峰的低浓度和微量样品的检测中发挥着重要作用. 图4(a)为Fe/zeolite-HT样品的可见拉曼光谱. 由图可见, Fe/mordenite-HT分子筛于402, 465, 800和830 cm^{-1}处出现四个特征峰, 均对应于mordenite的骨架振动[37~39];

Fe/beta-HT分子筛在320, 410, 470, 613, 700和830 cm^{-1}处出现六个特征峰, 其中320, 410和470 cm^{-1}处特征峰分别归属于六元环、五元环和四元环的呼吸振动[40]; 830 cm^{-1}处特征峰则来自分子筛骨架中Si–O的伸缩振动[41]; 613和700 cm^{-1}处的特征峰可能来自氧化铁或氢氧化铁中Fe–O的伸缩振动[42]或者beta分子筛晶体周围无定形SiO_2中Si–O键的伸缩振动[43,44]. ZSM-35分子筛骨架振动的特征峰出现在325, 425, 800和830 cm^{-1}处[43,45~48]; Fe/ZSM-5-HT分子筛除了在295, 380, 460和800 cm^{-1}处出现归属于MFI结构的特征峰以外, 还在526 cm^{-1}处出现特征峰, 可归属于低聚的FeO_x小簇中Fe–O–Fe的对称伸缩振动[22,49].

将Fe/zeolite-HT样品在523 K下暴露在5.0% N_2O/He气氛中之后, Fe/ZSM-5-HT和Fe/beta-HT分子筛在867 cm^{-1}处, Fe/ZSM-35-HT分子筛在730 cm^{-1}处出现新的特征拉曼谱峰(见图4(b)), 可分别归属于双核铁稳定的过氧物种中(O–O)的对称伸缩振动[34]和双核$Fe_2(\mu\text{-}O)_2$物种中(O–Fe–O)的对称伸缩振动[23]. Fe/mordenite-HT分子筛上则几乎观察不到双核铁物种形成.

3.5. 铁活性位的浓度

采用瞬态应答方法测定了Fe/zeolite-C/HT样品上铁活性位的浓度. 图5为Fe/ZSM-5-HT样品在1173 K下He中预处理1 h后, 再切换成5.0% N_2O/He时的产物-时间应答曲线. 可以看出, 在尾气中只检测到了N_2和N_2O, 表明N_2O在523 K分解后生成的氧物种落在了Fe/zeolite样品的表面上. 用Fe/zeolite-C样品进行瞬态应答实验则几乎观察不到N_2的生成, 说明高温处理是铁活性位生成的一个必要条件[22]. 通过计算生成N_2的积分面积可以得到单位质量Fe/zeolite样品中铁活性位的浓度, 结果见表2. 可以看出, Fe/zeolite-HT样品上铁活性位的浓度高低顺序为 Fe/ZSM-35-HT > Fe/beta-HT > Fe/ZSM-5-HT > Fe/mordenite-HT. 这与FT-IR结果一致, 即1874 cm^{-1}处红外谱峰的强度随着铁活性位浓度的增加而线性增加(见图5(b)). 结合原位FT-IR谱, 可见拉曼光谱及瞬态应答实验的结果可知, 在Fe/ZSM-35-HT, Fe/ZSM-5-HT和Fe/beta-HT样品中,骨架外铝稳定的双核铁物种是低温N_2O分解的活性中心. 在瞬态应答实验中, Fe/mordenite-HT上只有少量N_2生成, 这进一步证明在Fe/mordenite-HT分子筛上几乎不存在低聚的铁物种.

3.6. Fe/zeolite样品的催化性能

图6(a)为Fe/zeolite-C/HT样品在N_2O分解反应中N_2O转化率随温度的变化. 由图可见, 对于Fe/ZSM-35-C, Fe/ZSM-5-C和Fe/beta-C催化剂样品, N_2O在700 K以上有明显的转化, 至773 K时完全分解. Fe/mordenite-C样品上N_2O的分解反应从743 K开始, 到853 K完成. N_2O在773 K时分解速率的大小顺序为Fe/ZSM-35-C > Fe/ZSM-5-C > Fe/beta-C > Fe/mordenite-C (见表2), 并且N_2O的分解速率随着Fe/zeolite样品中孤立与寡聚铁物种总含量的增加而线性增加(见图7(a)). 这表明在Fe/zeolite-C样品中, 除较大的氧化铁纳米颗粒外的各种铁物种都对N_2O分解反应有贡献.

高温处理使所有Fe/zeolite样品的催化活性显著提高, 结果见图6(b). N_2O转化率达到50%时所需温度与Fe/zeolite-C样品上相比, Fe/ZSM-35, Fe/beta, Fe/ZSM-5和Fe/mordenite样品上分别降低了80, 50, 40和30K. Fe/zeolite-HT样品在713 K时N_2O分解活性顺序为: Fe/ZSM-35-HT > Fe/beta-HT > Fe/ZSM-5-HT > Fe/mordenite-HT, 且N_2O的分解速率随双核铁物种浓度的增加而线性增加(见图7(b)). 这说明骨架外铝稳定的双核铁物种是Fe/ZSM-35-HT, Fe/ZSM-5-HT和Fe/beta-HT催化剂中稳态N_2O分解的活性中心. 由于Fe/mordenite-HT分子筛上很难形成这种特殊结构的双核铁物种, 所以其高温处理前后在N_2O分解反应中的催化性能相差无几.

Fe/zeolite-HT样品在N_2O分解反应活性上的差别与双核铁物种的浓度有关, 而双核铁物种的形成与分子筛的种类又密切相关. 离子交换法制备的分子筛样品中, 二价过渡金属阳离子一般落在分子筛中的α, β和γ型阳离子位上[9]. 图8是FER, MFI, BEA和MOR分子筛中α, β和γ型阳离子位. 其中α位位于两个五元环形成的六元环中, 它位于MOR, FER和ZSM-5分子筛十元环直孔道壁上以及BEA结构分子筛的多形体C中; β位位于MOR腔中扭曲的八元环中、FER腔中扭曲的六元环中、MFI结构分子筛直孔道和Z型孔道交叉处的六元环中以及BEA结构分子筛多形体A和B的六边形笼中的平面扭曲的六元环中; γ位位于FER, MFI和MOR中的船型位中和BEA结构分子筛多形体A和B的六边形笼中.

Dědeček课题组[50,51]研究发现, 在Co/zeolites催化剂体系中, 只有落在α和β位上的Co(II)离子才能参与反应, 落在γ位上的Co(II)离子不能参与反应. 高温处理的Fe/zeolite样品上形成的双核铁位中的铁物种是Fe(II), 而不是Fe(III), 并且二价过渡金属阳离子在高硅分子筛中的落位具有普适性. 此外, 一般认为, O_2的脱附是N_2O分解反应的决速步骤[25], 相邻两个铁活性位之间较短的距离更有利于表面氧物种的结合与脱附. 因此, Fe/zeolite

样品中相邻两个铁活性位之间的距离与其催化活性密切相关. 分子筛中相邻两个α位或相邻两个β位的距离可以认为代表了相邻最近的两个Fe(II)离子的距离. 不同分子筛中相邻两个α位或相邻两个β位的距离是不同的. ZSM-35中相邻两个α位和相邻两个β位的距离分别是0.54 nm和0.61 nm [50]. ZSM-5中相邻两个α位的距离是0.75 nm, 但它们不是面对面存在的, 由此形成的双核铁位不利于N_2O分解反应的进行. 相邻两个β位的距离是0.45 nm并且它们处在直孔道与Z型孔道的交叉处, 有利于N_2O分解过程中反应物和产物的扩散[10]. Beta分子筛中落在多形体C中α位上的Fe(II)离子不能参与反应. Beta分子筛中相邻两个β位的距离是0.75 nm, 它们位于多形体A和B中六边形笼的平面扭曲的六元环中心, 有利于N_2O分解反应中过渡态的形成, 所以只考虑落在多形体A和B中相邻两个β位上的两个Fe(II)离子[8].

综上可知, 落在ZSM-35分子筛十元环直孔道中相邻两个α位上的两个Fe(II)离子和八元环孔道中相邻两个β位上的两个Fe(II)离子都容易形成双核铁位; 落在beta分子筛多形体A和B中六边形笼中相邻两个β位上的两个Fe(II)离子容易形成双核铁位; 落在ZSM-5分子筛十元环直孔道与Z型孔道交叉处相邻两个β位上的两个Fe(II)离子容易形成双核铁活性位.

另外一个能控制高硅分子筛中铁活性位形成的因素是特定的阳离子位上成对铝的分布[10,52]. 因为双核铁活性位的形成需要在两个相邻阳离子位上的每个阳离子位中都存在两个铝原子, 所以成对铝的分布能控制分子筛中铁物种的结构和浓度[10,52]. Dědeček等[15~19]以Co(II)离子为探针, 利用紫外-可见漫反射光谱测定了分子筛中特定阳离子位上成对铝存在的最大量.

ZSM-35分子筛中, Co(II)离子的最大交换量是Co/Al = 0.31, 所有的骨架Al原子中大约62%是以成对的形式分布在α和β位的六元环中[10]. Si/Al = 10.5的ZSM-35分子筛中, 单位质量的催化剂中有7.9×10^{-4} mol/g 的Al原子. Fe/Al = 0.33时, 单位质量催化剂中有4.9×10^{-4} mol/g的Al原子以成对的形式存在于α位和β位的六元环中($7.9 \times 10^{-4} \times 0.62$). Fe/ZSM-35分子筛中, 大约有5%和85%的Fe(II)离子分别落在分子筛的α位和β位上[18], 并且相邻两个α位和相邻两个β位上都可以形成双核铁位. 因此, 单位质量催化剂中平均有2.5×10^{-4} mol/g的铁离子可以形成双核铁位. 对于Si/Al = 13的beta分子筛而言, 最大Co/Al比为0.45 (大约有90%的骨架Al以成对的形式存在于六元环中), 55%的Co(II)离子落在β位上[17]. Fe/Al = 0.33时, 单位质量催化剂中有3.2×10^{-4} mol/g 的Al原子以成对的形式存在于β位上, 则单位催化剂中可以形成双核铁位的Fe(II)离子的量为1.6×10^{-4} mol/g. ZSM-5中最大的Co/Al比为0.4, 因此80%的骨架Al原子以成对的形式存在于六元环上, 其中50%的Al落在β位上[53]. 也就是说, 最多有40%的骨架Al原子落在β位的六元环上. Si/Al = 12.5的ZSM-5分子筛中, 单位质量催化剂中有6.7×10^{-4} mol/g 的Al原子; Fe/Al = 0.33时, 单位质量催化剂中有2.7×10^{-4} mol/g 的Al原子以成对的形式存在于β位上, 则单位质量催化剂中可以形成双核铁位的Fe(II)离子的量为1.3×10^{-4} mol/g. 总之, 在Fe/ZSM-35-HT, Fe/beta-HT和Fe/ZSM-5-HT分子筛中双核铁活性位的浓度顺序是Fe/ZSM-35-HT > Fe/beta-HT > Fe/ZSM-5-HT, 与它们催化N_2O分解活性顺序一致.

4. 结论

采用紫外-可见漫反射光谱、原位红外光谱及可见拉曼光谱并结合瞬态应答方法研究了不同Fe/zeolite样品在N_2O分解反应中的催化性能. 结果表明, Fe/zeolite-HT样品在N_2O分解反应中的活性顺序为Fe/ZSM-35-HT > Fe/beta-HT > Fe/ZSM-5-HT > Fe/mordenite-HT, 与骨架外铝稳定的双核铁物种的浓度呈线性关系. 这说明Fe/ZSM-35-HT, Fe/beta-HT和Fe/ZSM-5-HT催化剂上形成的双核铁位是N_2O分解的活性中心. Fe/mordenite-HT中的Fe物种主要以孤立铁离子的形式存在, 因此其在N_2O分解反应中的催化活性很低. 这种双核铁物种的形成与分子筛的种类又是密切相关的. 结果表明, Fe/ZSM-35分子筛十元环孔道中相邻两个α位和八元环孔道中相邻两个β位都能稳定两个Fe(II)离子而形成能高效分解N_2O的双核铁活性中心. Fe/beta和Fe/ZSM-5分子筛中只有落在相邻两个β位上的两个Fe(II)离子才能形成参与N_2O分解的高活性的双铁活性中心.